Supporting Information

Laser-Driven Phase Segregation and Tailoring of Compositionally Graded Microstructures in Si-Ge Nanoscale Thin Films

Ozan Aktas[*,†], Swe Z. Oo[†,‡], Stuart J. MacFarquhar[†], Vinita Mittal[†], Harold M. H. Chong[‡,§], and Anna C. Peacock*[*,†]*

[†]Optoelectronics Research Centre, University of Southampton, Southampton, SO17 1BJ, UK

[‡]School of Electronics and Computer Science, University of Southampton, Southampton, SO17 1BJ, UK

[§]School of Materials Science, Japan Advanced Institute of Science and Technology, Ishikawa, 923-1292, Japan

*E-mail: O.Aktas@soton.ac.uk

*E-mail: acp@orc.soton.ac.uk

This PDF file includes:

Supporting Information (SI) Sections S1 to S6
Figures S1 to S13
Tables S1 to S2
Legends for Movies S1 to S2
SI References

Other Supporting Information materials:

Movies S1 to S2

SI Figures

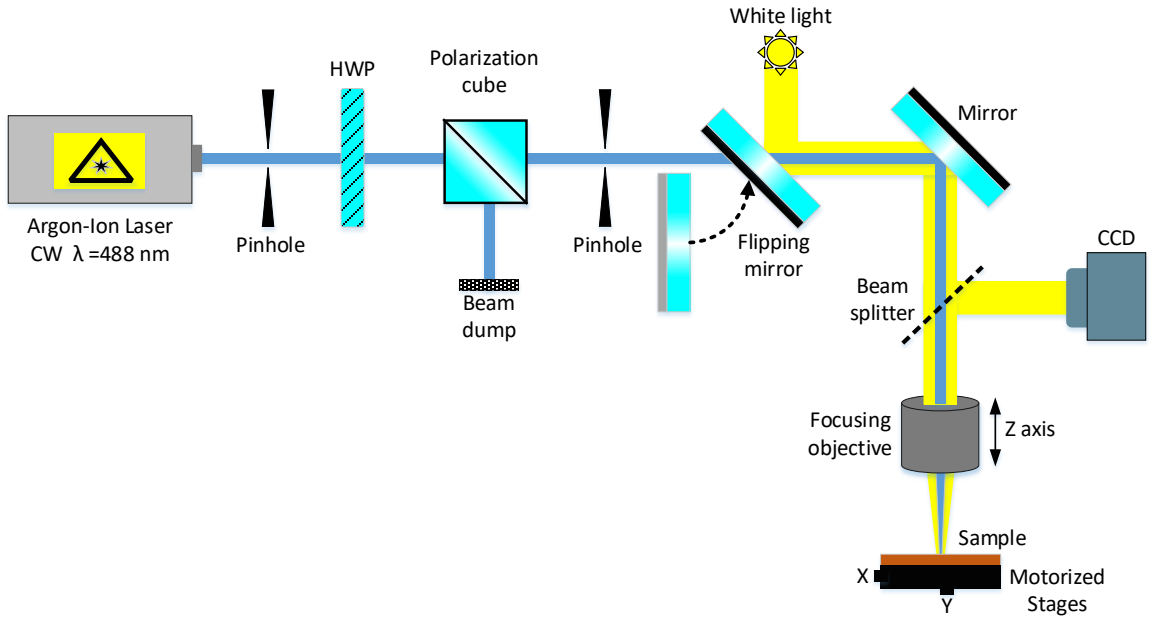

Figure S1: Experimental setup for laser processing of a-SiGe thin films. Schematic of the experimental setup used for laser processing of SiGe thin films on Si substrates. The light source is an Argon ion laser emitting continuous wave (CW) radiation at 488 nm with a maximum power of 320 mW, as measured with a power detector after the focusing objective. To avoid distortion in the laser beam, we adjusted the optical power by using a polarization cube and a half-wave plate (HWP). The laser beam was focused on the top surface of the amorphous SiGe thin film using either a 10X objective lens or a 20X lens to produce spots sizes of diameter 7 μm or 3 μm, respectively. A flip mirror was used to couple broadband white light into the optical path, and a CCD camera was used to image the surface before and after the laser processing. Samples were mounted with a vacuum holder on software-controlled motorized stages, which are capable of precision movements in three dimensions. These stages were used to scan the sample under the laser beam at speeds ranging from 0.01 to 100 mm s^{-1}. The power was adjusted between 200 mW and 320 mW. High temperatures, sufficient to melt the amorphous semiconductor, can be reached due to the high optical absorption in the visible spectrum. Localized melting and solidification induce compositional segregation in SiGe films as well as structural modification, and volume reduction due to the higher density of polycrystalline SiGe.

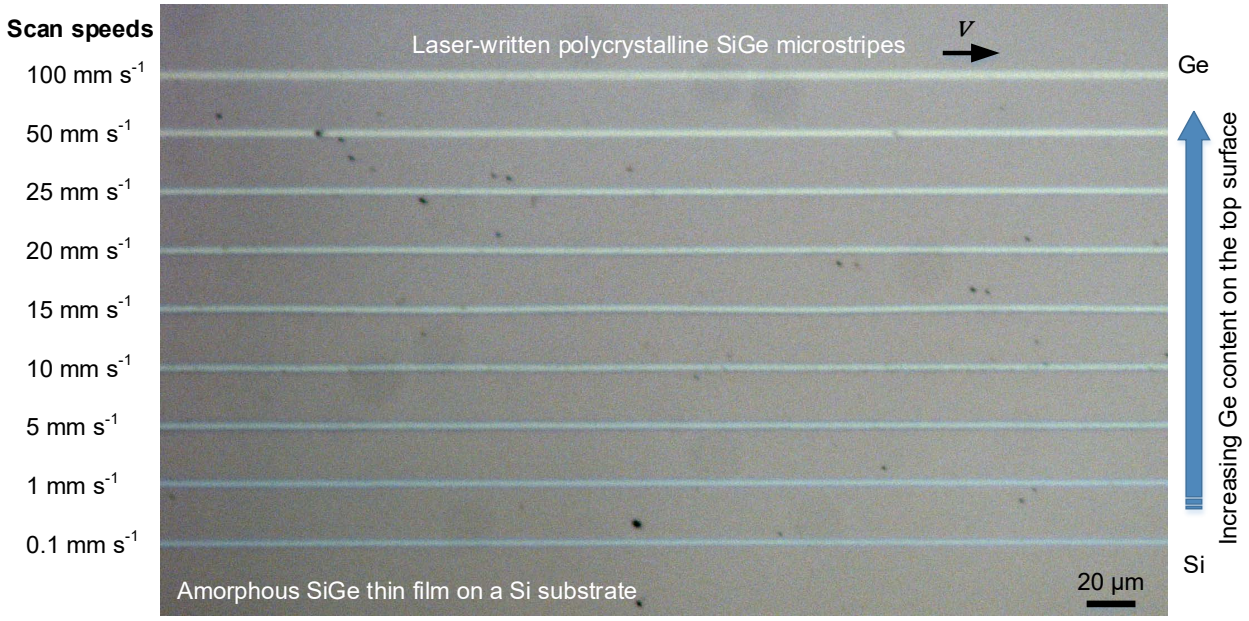

Figure S2: **Laser-driven phase segregation in the laser-written SiGe microstripes.** Optical microscope image taken at 20X magnification shows the highly reflective surfaces of the 3 µm wide laser-written polycrystalline silicon-germanium (poly-SiGe) microstripes on an amorphous silicon-germanium (a-SiGe) thin film for different laser scan speeds. The blue to yellow color shading indicates a scan-speed-dependent $Si_{1-x}Ge_x$ composition redistribution. Laser heating induces a travelling molten zone that drags a Ge-rich liquid in the direction of scanning and redistributes the $Si_{1-x}Ge_x$ composition depending on the scan speed during solidification. Higher scan speeds result in higher Ge content on the top surface with the build-up of Ge atoms on the trailing edge of the molten zone, due to the diffusion-limited solute transport. Tunable Ge contents on the top surface are thus available during the scanning of the laser beam.

SI Section S1 - Calculation of phase diagram for SiGe alloy and determination of the regular solution parameters by fitting to the experimental data

The molar Gibbs free energy *G(ϕ, T, x)* of a $Si_{1-x}Ge_x$ alloy,[1] which is assumed to behave as a regular solution, is given at a constant pressure by

$$G = (1-x)G_{Si}(\phi, T) + xG_{Ge}(\phi, T) + RT[(1-x)\ln(1-x) + xlnx] + w(\phi)x(1-x), \quad (1)$$

where *x* is the molar fraction of Ge, *R* is the ideal gas constant, *T* is the temperature, ϕ is the phase-field parameter representing smooth transitions between solid (ϕ = 0) and liquid (ϕ = 1) phases. $G_{Si}(\phi, T)$ and $G_{Ge}(\phi, T)$ are the Gibbs free energy functions of pure silicon and germanium, respectively. The Gibbs free energy function representing both liquid and solid phases of a pure element A (Si or Ge) is given by

$$G_A(\phi, T) = H_A \mathrm{g}(\phi) + L_A\left(1 - \frac{T}{T_m^A}\right)p(\phi), \quad (2)$$

where H_A is the height of the energy barrier between the liquid and solid phases at the melting temperature T_m^A of the pure element A; L_A is latent heat of melting; $\mathrm{g}(\phi) = \phi^2(1-\phi)^2$ is the double-well potential function with minima at $\phi = 0$ and $\phi = 1$; and $p(\phi) = \phi^2(3-2\phi)$ is an interpolating function, which satisfies $p(\phi = 0) = 0$ and $p(\phi = 1) = 1$. The height of the energy barrier H_A was assumed the same for Si and Ge. The first two terms and the third term in equation (1) emerge from enthalpic and entropic interactions, respectively. The last term is the molar excess Gibbs free energy for a regular solution, and $w(\phi)$ is a phase-dependent regular solution function given by

$$w(\phi) = w_S(1-\phi) + w_L\phi, \quad (3)$$

where w_S and w_L are regular solution parameters corresponding to solid and liquid phases of SiGe alloy, respectively.

The chemical potentials for silicon and germanium can be calculated from the molar Gibbs energy function *G(ϕ, T, x)* in equation (1) as

$$\mu_{Si} = G - x\frac{\partial G}{\partial x} = w(\phi)x^2 + G_{Si}(\phi, T) + RT\ln(1-x), \quad (4)$$

$$\mu_{Ge} = G + (1-x)\frac{\partial G}{\partial x} = w(\phi)(1-x)^2 + G_{Ge}(\phi, T) + RT\ln(x). \quad (5)$$

When there is a phase coexistence at thermal equilibrium, the chemical potential in the solid (S) and liquid (L) solutions should be equal for each element, as given by

$$\mu_{Si}^S(\phi = 0, T, x_S) = \mu_{Si}^L(\phi = 1, T, x_L), \quad (6)$$

$$\mu_{Ge}^S(\phi = 0, T, x_S) = \mu_{Ge}^L(\phi = 1, T, x_L), \quad (7)$$

where x_S and x_L are Ge molar fraction in the solid and liquid solutions of $Si_{1-x}Ge_x$, respectively. Using equations (2-5), the thermal equilibrium conditions for chemical potentials of Si and Ge in equations (6,7)

can be rewritten explicitly in terms of the regular solution parameters, latent heats of melting and melting temperatures of the elements,[2,3] as given below

$$ln\frac{1-x_S}{1-x_L} = \frac{L_{Si}}{R}\left(\frac{1}{T} - \frac{1}{T_m^{Si}}\right) + \frac{1}{RT}(w_L x_L^2 - w_S x_S^2), \quad (8)$$

$$ln\frac{x_S}{x_L} = \frac{L_{Ge}}{R}\left(\frac{1}{T} - \frac{1}{T_m^{Ge}}\right) + \frac{1}{RT}[w_L(1-x_L)^2 - w_S(1-x_S)^2], \quad (9)$$

which permit calculation of the liquidus and solidus lines in the phase diagram of SiGe (Supporting Information Figure S3), corresponding to x_L vs *T* and x_S vs *T*, respectively. The parameters that fit best to the experimental phase diagram of SiGe alloys, data for which is given in Supporting Information Table S1, are $T_m^{Si} = 1687$ K, $L_{Si}/R = 6040$ K, $T_m^{Ge} = 1211$ K, $L_{Ge}/R = 4441$ K, $w_S/R = 450$ K and $w_L/R = 800$ K.

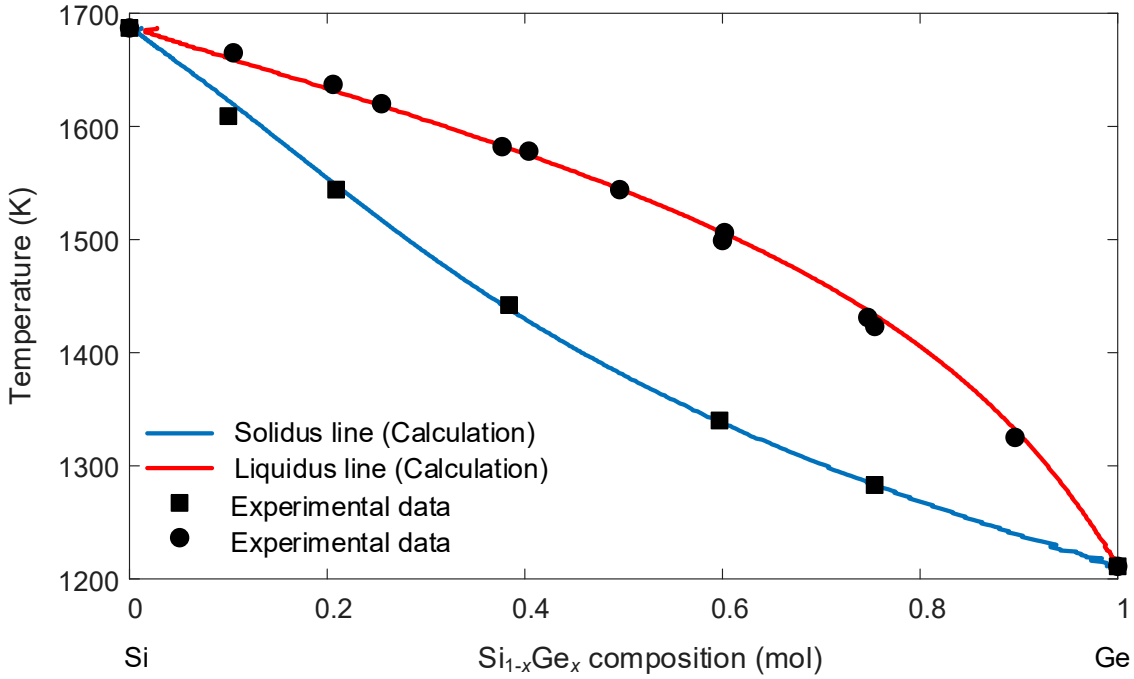

Figure S3: **Experimental and theoretical phase diagram of SiGe alloy.** Phase diagram of SiGe alloy shows theoretically calculated liquidus (red) and solidus (blue) lines, which were obtained as the best fits to the experimental composition vs temperature data reported in the literature[4] (see Supporting Information Table S1). A regular solution model for the SiGe alloy was assumed for the calculation of its phase diagram from the Gibbs free energy (see Supporting Information Section S1).

SI Section S2 - Derivation of the generalized nonlinear diffusion equation for phase segregation

Our laser heating process, which employs a continuous wave (CW) source with a spot diameter of 3 μm and scan speeds in the range of 0.1-100 mm s^{-1}, has an average dwell time of ~100 μs. On the other hand, the local temperature distribution reaches thermal equilibrium almost instantly, in a duration less than 1 μs during the laser scanning. Therefore, we applied a quasi-isothermal treatment to find a generalized diffusion equation that incorporates the phase segregation of SiGe binary alloys melted by lasers. An isothermal treatment assumes a phase-field parameter $\phi(\vec{r},t)$ representing the laser-induced travelling molten zone with a smooth solid/liquid interface, and a free energy density functional $g(\phi,T,x)$ that globally minimizes the integral taken over the whole SiGe film volume, as given by[5]

$$I = \int \left[g(\phi,T,x) + \frac{\varepsilon_\phi^2}{2} |\nabla\phi|^2 \right] dV, \tag{10}$$

where T is the temperature distribution, x is the molar fraction of Ge in $Si_{1-x}Ge_x$, and ε_ϕ is a parameter related to the length scale and energy of the solid/liquid interface. The free energy density functional is taken as

$$g(\phi,T,x) = \frac{G(\phi,T,x)}{V_m}, \tag{11}$$

where $G(\phi,T,x)$ is the molar Gibbs free energy given in equation (1), divided by the molar volume V_m. At equilibrium, all variational derivatives of equation (10) are equal to zero.

For time-dependent non-steady state, the total free energy always decreases by the following phase-field equations

$$\frac{\partial\phi}{\partial t} = -M_\phi \left[\frac{\partial g}{\partial\phi} - \varepsilon_\phi^2 \nabla^2\phi \right], \tag{12}$$

$$\frac{\partial x}{\partial t} = \nabla \cdot \left[M_x \nabla \left(\frac{\partial g}{\partial x} \right) \right], \tag{13}$$

where M_ϕ and M_x are positive mobilities related to the interface kinetic coefficient and the diffusion coefficient. Equation (13) guarantees the conservation of the solute atoms in the total volume. Although equation (12) and (13) are coupled through the free energy density functional $g(\phi,T,x)$, we assumed that the thermal properties of the SiGe alloy such as melting temperature and thermal conductivity are determined by the initial composition x_0 and stay constant during the simulations. This assumption not only simplified the problem but also enabled us to solve the time-dependent equation (12) with the Heat Transfer Module in COMSOL software, which provides the phase-field parameter $\phi(\vec{r},t)$. However, equation (13) was solved as being coupled to the phase-field parameter $\phi(\vec{r},t)$, using the Stabilized Convection-Diffusion Equation Module.

M_x in equation (13), is given by[6]

$$M_x = \frac{D(\phi)}{\partial^2 g(\phi,T,x)/\partial^2 x} = \frac{V_m D(\phi)(1-x)x}{RT - 2x(1-x)w(\phi)}, \tag{14}$$

in terms of the phase-dependent diffusion coefficient

$$D(\phi) = D_S(1-\phi) + D_L\phi, \tag{15}$$

where the diffusion coefficient in the liquid and solid phases are taken as D_L = 3.0×10^{-8} m^2 s^{-1} and D_S = 0, respectively. Equations (11) and (14) are inserted in equation (13) to find the generalized nonlinear diffusion equation

$$\frac{dx}{dt} = \nabla[D(\phi)\nabla x] + \nabla\left[D(\phi)(1-x)x\frac{\left[\frac{L_{Ge}}{R}\left(1-\frac{T}{T_m^{Ge}}\right)-\frac{L_{Si}}{R}\left(1-\frac{T}{T_m^{Si}}\right)+(1-2x)\left(\frac{w_L-w_S}{R}\right)\right]}{T-2(1-x)x\left[\frac{w_S}{R}(1-\phi)+\frac{w_L}{R}\phi\right]}\frac{\partial p(\phi)}{\partial\phi}\nabla\phi\right], \tag{16}$$

where the derivative of the interpolating function $p(\phi)$ is $p'(\phi) = 6(1-\phi)\phi$. The second term on the right hand side of equation (16) drives the compositional segregation of Si and Ge *via* the gradient $\nabla\phi$ of the phase-field parameter ϕ, which has the highest value at the solid/liquid (S/L) interface in the molten zone. When $\nabla\phi = 0$, i.e., away from the S/L interface, the standard diffusion equation is obtained in the solid and liquid domains, as the concentration C is related to the Ge molar fraction x by $C = x/V_m$.

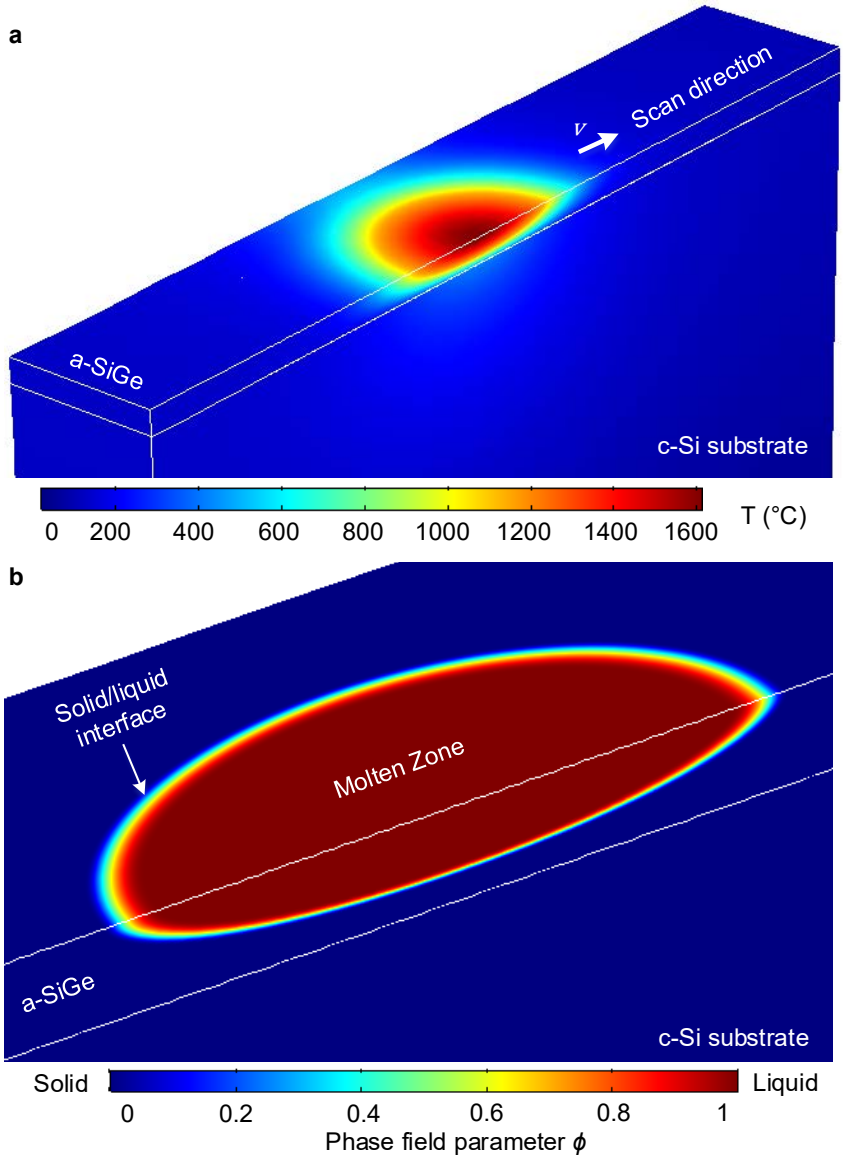

Figure S4: **Temperature distribution and laser-induced travelling molten zone. a)** Laser heating by the absorption of visible radiation results in a localized Gaussian-like temperature distribution on the surface of the SiGe film with a thickness of 400 nm. Temperatures as high as 1,600 °C can be reached during laser processing with high-temperature gradients (10^9 K m^{-1}) and high cooling rates (10^5 K s^{-1}). **b)** Travelling molten zone with a semi-elliptical cross-section is represented by a phase-field parameter ϕ showing transitions between solid to liquid phases with a smooth interface, which corresponds to the mushy region between liquidus and solidus lines in the phase diagram of SiGe alloy. The gradient $\nabla\phi$ of the phase-field parameter ϕ, reaches a maximum value at the solid/liquid interface at the bottom of the molten zone, where the maximum phase segregation occurs.

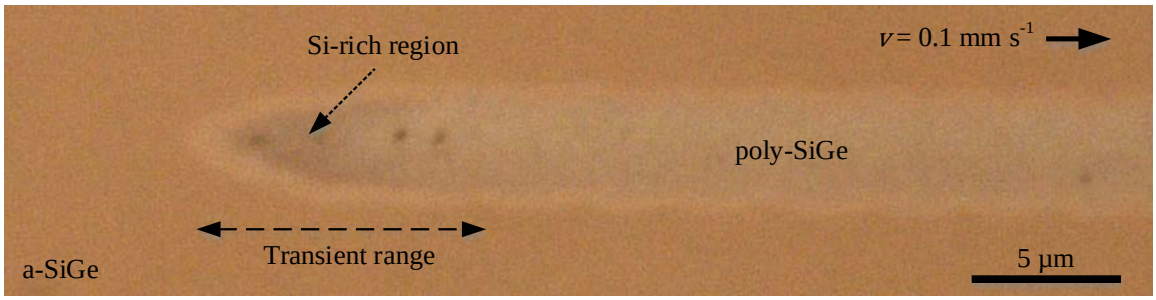

Figure S5: **Experimental observation of the initial transient region during laser processing.** The optical microscope image shows the initial transient evolution of composition *x* through the laser-written microstripe on an amorphous $Si_{0.4}Ge_{0.6}$ film processed at a scan speed of 0.1 mm s^{-1}. Darker area in the transient region indicates Si-rich SiGe alloy. This experimentally observed initial transient region in the Ge composition agrees well with the simulations based on the generalized nonlinear diffusion equation given in in equation (16).

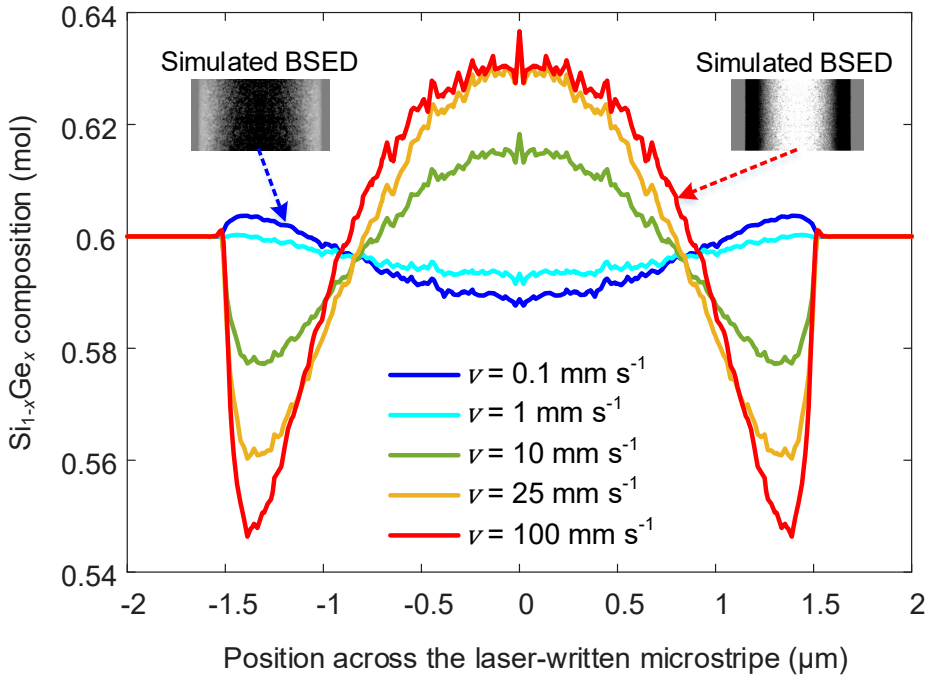

Figure S6: Transverse profiles of the surface-normal-averaged Ge molar fraction. Figure shows the transverse profiles of the numerically calculated back-scattered electron detector images (BSED) for the steady-state regions of the 3 μm wide laser-written poly-SiGe microstripes. The two inset figures show the corresponding simulated 2D BSED micrographs for the 0.1 and 100 mm s^{-1} scan speeds. The surface-normal averaged Ge composition <*x*> increases at the centre of the laser-written stripes and saturates at the scan speed of 25 mm s^{-1}, while the width of the darker regions continue increasing at higher scan speeds. The increase of Ge in the Ge-rich strip core is compensated by the decrease of Ge in the Si-rich under-cladding, resulting in the saturation of the average composition at the centre (brighter) and widening of the widths in the Si-rich regions (darker).

SI Section S3 - Calculation of critical velocity of solidification

Directional solidification theories predict a critical solidification velocity for the onset of interface instability in alloys, which is given by[7]

$$v_c = \frac{|\nabla T| D}{\Delta T_0}, \quad (17)$$

where $|\nabla T|$ is the thermal gradient ahead of the solidification front, D is the solute diffusivity, and ΔT_0 is the mushy zone range for an alloy of overall solute concentration x_0. Using simulations, we estimated the thermal gradient at the trailing edge of the molten zone to be $|\nabla T| = 0.45 \times 10^9$ K m^{-1}. The diffusion coefficient for elemental Ge in molten SiGe is $D_L = 3.0 \times 10^{-8}$ m^2 s^{-1}. The temperature difference between the liquidus and solidus lines is found to be ΔT_0 = 169 K at the initial overall composition of x_0 = 0.6 (Supporting Information Figure S3). When all known values are inserted in equation (17), the critical solidification velocity for SiGe films on Si substrates is found to be 79.9 mm s^{-1}.

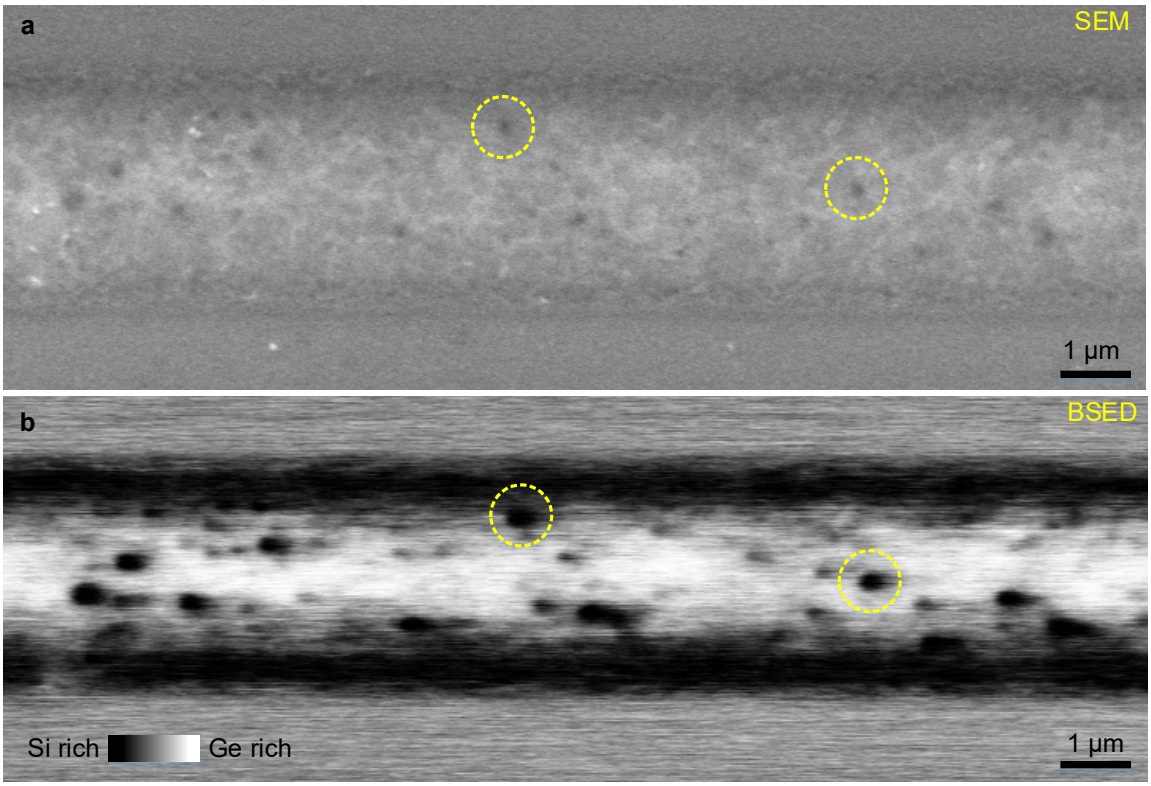

Figure S7: **Observation of Si-rich nanoparticles within a laser-written SiGe microstripe processed at 100 mm s^{-1}. a,b)** Scanning electron microscope (SEM) and back-scattered electron detector (BSED) micrographs show (**a**) structural and (**b**) material contrast for a polycrystalline SiGe stripe written at a scan speed of 100 mm s^{-1}. We observed Si-rich nanoparticles dispersed within the laser-treated region after laser processing. Yellow-circled regions highlight darker nano-domains, which correspond to a Si-rich SiGe alloy.

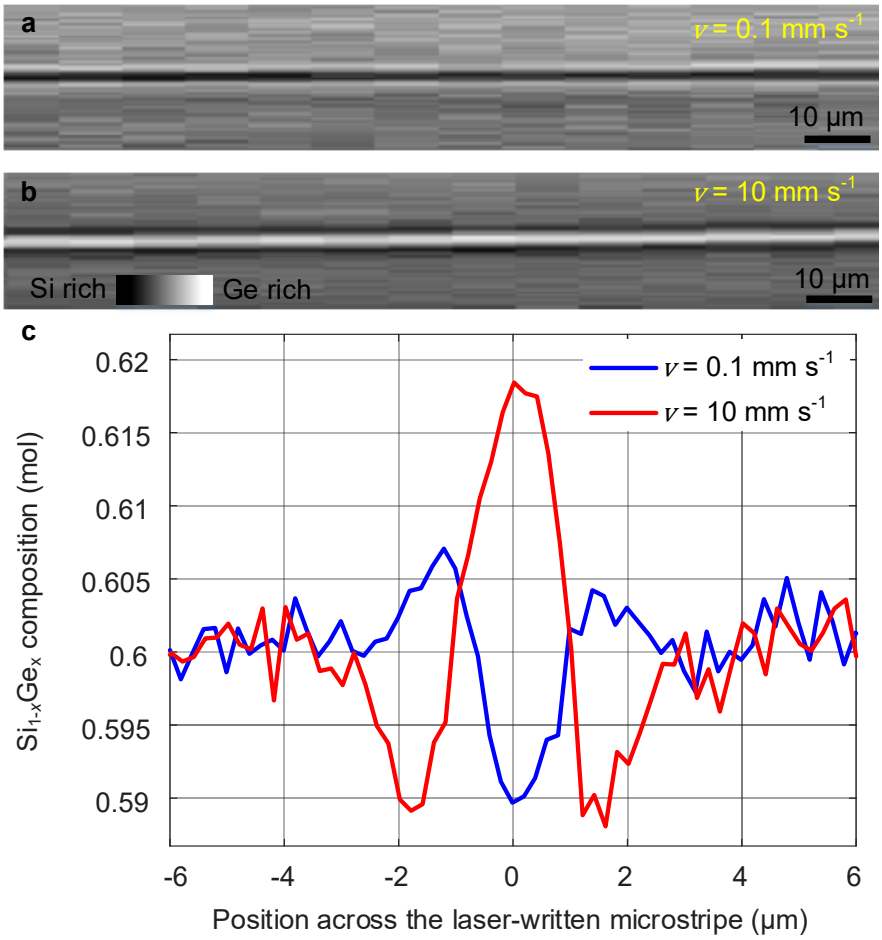

Figure S8: **X-ray Fluorescence (XRF) Spectroscopy on the laser-written SiGe microstripes. a,b)** XRF images the show intensity of Ge $K\alpha_1$ (9.886 keV) fluorescence emissions from the 7 μm wide poly-SiGe stripes laser-written at scan speeds of (**a**) 0.1 mm s^{-1} and (**b**) 10 mm s^{-1}. A collimated 11.0 keV X-ray beam of size 2×30 μm was raster scanned in 0.2 μm and 10 μm steps across and along the laser-written stripes, respectively. **c)** 1D XRF intensity profiles of the transverse cross-sections, plotted as a function of position across the laser-written stripes. The data were calibrated using the XRF intensity of the amorphous regions on the SiGe films, whose Ge compositions *x* were known. Narrowband detection of Ge $K\alpha_1$ in the X-ray spectrum is directly sensitive to the amount of Ge content *x*; however, due to the comparable transverse size of the X-ray beam and width of the laser-written stripes, only volume averaged Ge compositions $\langle x \rangle$ can be measured, underestimating the composition gradients and the peak composition values in the 1D XRF profiles.

SI Section S4 - Composition and strain estimations from Raman spectra

Three Voigt profiles are fitted to the Raman peaks corresponding to the Si-Si, Si-Ge and Ge-Ge vibration modes, to identify their positions ω in the Raman spectra, which are bilinear functions of Ge composition *x* and in-plane strain $\epsilon_{\parallel}$ in the SiGe alloy, as given by[8-11]

$$\omega^{\mathrm{SiSi}} = \omega_0^{\mathrm{SiSi}} + A^{\mathrm{SiSi}}x + b^{\mathrm{SiSi}}\epsilon_{\parallel}, \tag{18a}$$

$$\omega^{\mathrm{SiGe}} = \omega_0^{\mathrm{SiGe}} + A^{\mathrm{SiGe}}x + b^{\mathrm{SiGe}}\epsilon_{\parallel}, \tag{18b}$$

$$\omega^{\mathrm{GeGe}} = \omega_0^{\mathrm{GeGe}} + A^{\mathrm{GeGe}}x + b^{\mathrm{GeGe}}\epsilon_{\parallel}, \tag{18c}$$

where ω^{SiSi}, ω^{SiGe}, ω^{GeGe} are the experimental peak positions; *x* is the Ge content in $Si_{1-x}Ge_x$; ω_0^{SiSi} = 520 cm^{-1}, ω_0^{SiGe} = 411 cm^{-1}, ω_0^{GeGe} = 280 cm^{-1} are the reference (unstrained) peak positions. A^{SiSi}, A^{SiGe} and A^{GeGe} are the coefficients linking the ω-shift of the Si–Si, Si–Ge and Ge–Ge modes with Ge composition *x*, while b^{SiSi}, b^{SiGe} and b^{GeGe} are the Raman peak position shifts with the in-plane strain $\epsilon_{\parallel}$. The peak position of ω^{SiGe} cannot be written as a linear function of composition *x* for the full range 0 < *x* < 1, due to the presence of a turning point around *x*= 0.5 in the Raman spectra. In order to have a linear equation valid for *x* > 0.5, we take the unstrained peak position of ω_0^{SiGe}, as $x \to 0.5$. Following the procedure from Wang et al.,[12] *x* and $\epsilon_{\parallel}$ can be isolated from equation (18a) and (18c), and then substituted into equation (18b) to obtain an estimation for $\omega_{\mathrm{calc}}^{\mathrm{SiGe}}$ peak position in terms of the experimentally obtained ω^{SiSi} and ω^{GeGe} peak positions,

$$\omega_{\mathrm{calc}}^{\mathrm{SiGe}} = \omega_0^{\mathrm{SiGe}} + \frac{\left(A^{\mathrm{SiGe}}b^{\mathrm{GeGe}} - A^{\mathrm{GeGe}}b^{\mathrm{SiGe}}\right)\left(\omega^{\mathrm{SiSi}} - \omega_0^{\mathrm{SiSi}}\right) + \left(A^{\mathrm{SiSi}}b^{\mathrm{SiGe}} - A^{\mathrm{SiGe}}b^{\mathrm{SiSi}}\right)\left(\omega^{\mathrm{GeGe}} - \omega_0^{\mathrm{GeGe}}\right)}{A^{\mathrm{SiSi}}b^{\mathrm{GeGe}} - A^{\mathrm{GeGe}}b^{\mathrm{SiSi}}}. \tag{19}$$

A MATLAB script was used to minimize the total squared error between experimental ω^{SiGe} and calculated $\omega_{\mathrm{calc}}^{\mathrm{SiGe}}$ for the whole Raman datasets by altering the coefficients A^{SiSi}, A^{SiGe}, A^{GeGe}, b^{SiSi}, b^{SiGe} and b^{GeGe} in a range expected for each. After the determination of the optimum coefficients, which are $A^{\mathrm{SiSi}} = -75$, $A^{\mathrm{SiGe}} = -13$, $A^{\mathrm{GeGe}} = 19$, $b^{\mathrm{SiSi}} = -870$, $b^{\mathrm{SiGe}} = -550$, and $b^{\mathrm{GeGe}} = -510$, the set of equations (18) can be used to find the composition and strain values from the Raman Spectra. Equation (18) can be rewritten more succinctly in a matrix form

$$\Delta \mathrm{W} = \begin{pmatrix} \omega^{\mathrm{SiSi}} - \omega_0^{\mathrm{SiSi}} \\ \omega^{\mathrm{SiGe}} - \omega_0^{\mathrm{SiGe}} \\ \omega^{\mathrm{GeGe}} - \omega_0^{\mathrm{GeGe}} \end{pmatrix} = \begin{pmatrix} A^{\mathrm{SiSi}} & b^{\mathrm{SiSi}} \\ A^{\mathrm{SiGe}} & b^{\mathrm{SiGe}} \\ A^{\mathrm{GeGe}} & b^{\mathrm{GeGe}} \end{pmatrix} \begin{pmatrix} x \\ \epsilon_{\parallel} \end{pmatrix} = MX, \tag{20}$$

where M is the coefficient matrix, and X is the solution vector for the Ge content *x* and strain $\epsilon_{\parallel}$. A least-squares solution for this overdetermined set of equations can be calculated as

$$X = (M^{\perp}M)^{-1}M^{\perp}\Delta W, \tag{21}$$

where matrix inverse and transpose operations are applied to find the pseudo-inverse matrix.

SI Section S5 - Assessment of the unstrained lattice constants for the laser-written stripes of 0.1 mm s^{-1} *via* 2D strain analysis on the distortion of XRD rings

Laser processing creates residual biaxial tensile strains in the laser-written SiGe stripes, resulting in distorted XRD rings with an elliptical shape. Taking profiles in the azimuthal sectors, 2D diffractograms can be converted to a 2θ vs azimuthal angle α format, as showed in the Supporting Information Figure S9a. The slight decline in 2θ for each XRD ring corresponds to a change in the interplanar distance d_{hkl} over the range of the azimuthal angle α. To better visualize the lattice distortion, the lattice constant a of the strained SiGe alloy can be calculated by

$$a(\alpha) = \frac{\lambda\sqrt{h^2+k^2+l^2}}{2\sin(\theta(\alpha))}, \tag{22}$$

where λ is the wavelength of the X-ray beam, (*h k l*) are the Miller indices of the diffraction plane, and $2\theta(\alpha)$ is determined by the centre of the Gaussian peak fits to the XRD data at various azimuthal positions. The azimuthal dependency of the lattice constant $a(\alpha)$ can be seen in Supporting Information Figure S9b. The fits to the data were calculated by assuming a biaxial strain tensor in the form

$$\epsilon_{ij} = \begin{bmatrix} \epsilon_{xx} & \epsilon_{xy} & 0 \\ \epsilon_{xy} & \epsilon_{yy} & 0 \\ 0 & 0 & \epsilon_{zz} \end{bmatrix}, \tag{23}$$

where $\epsilon_{i,j}$ corresponds to the different components of the tensor with indices *i* and *j* running over *x*, *y*, and *z*. The sample and laboratory frames used for the strain analysis are displayed in the schematic of Supporting Information Figure S9c.

A diffraction vector $\vec{q}$ with the coordinates as a function of θ and α in the laboratory frame (x_L, y_L, z_L), can be transformed to the sample coordinate frame by a rotation of β around the common vertical axis y_L. Its coordinates (q_x, q_y, q_z) in the sample frame (x_S, y_S, z_S) are

$$\overrightarrow{q_s} = \begin{bmatrix} q_x \\ q_y \\ q_z \end{bmatrix} = \begin{bmatrix} cos\beta & 0 & -sin\beta \\ 0 & 1 & 0 \\ sin\beta & 0 & cos\beta \end{bmatrix} \begin{bmatrix} sin\theta \\ cos\theta sin\alpha \\ cos\theta cos\alpha \end{bmatrix}, \tag{24}$$

where β is the incident angle of the X-ray beam. Assuming the unstrained lattice constant a_0 of the material is known, the strain measured for a (*h k l*) plane along the diffraction vector $\overrightarrow{q_s}$

$$\epsilon_{hkl} = \frac{a-a_0}{a_0} = \frac{\lambda\sqrt{h^2+k^2+l^2}}{2a_0 sin\theta} - 1 \tag{25}$$

can be expressed in terms of the strain tensor components $\epsilon_{i,j}$ in the sample frame as[13]

$$\epsilon_{hkl} = \sum_{i,j} q_i q_j \epsilon_{ij} = q_x^2\epsilon_{xx} + q_y^2\epsilon_{yy} + q_z^2\epsilon_{zz} + 2q_x q_y \epsilon_{xy}. \tag{26}$$

Equation (26) can be written as a system of equations for *n* different XRD peaks on the Debye rings corresponding to different (*h k l*) planes and azimuthal angles α, which is given in a matrix format by

$$S = \begin{bmatrix} \epsilon_{hkl}(1) \\ \vdots \\ \epsilon_{hkl}(n) \end{bmatrix} = \begin{bmatrix} q_x^2(1) & q_y^2(1) & q_z^2(1) & 2q_x(1)q_y(1) \\ \vdots & \vdots & \vdots & \vdots \\ q_x^2(n) & q_y^2(n) & q_z^2(n) & 2q_x(n)q_y(n) \end{bmatrix} \begin{bmatrix} \epsilon_{xx} \\ \epsilon_{yy} \\ \epsilon_{zz} \\ \epsilon_{xy} \end{bmatrix} = N\epsilon, \quad (27)$$

where we define *S* and *N* as an *n*×1 strain data vector and an *n*×4 data matrix, respectively. The unknown strain tensor ϵ can be found as a least-squares solution for the overdetermined set of equations (27), which is given as

$$\epsilon = N^{-1}S, \quad (28)$$

where N^{-1} represents the pseudo-inverse matrix of *N*.

Since the unstrained lattice constant a_0 is generally not known, or the value inaccurate, an approximate lattice constant $\tilde{a}_0 = a_0 + \delta a$ can be alternatively considered. Replacing the real a_0 with the $\tilde{a}_0$ will always result in a hydrostatic strain component in the strain data vector S, the n^{th} component of which can be derived from equation (25) as

$$S(n) = S_0(n) - \frac{\lambda\sqrt{h^2+k^2+l^2}}{2sin\theta(n)}\frac{\delta a}{a_0^2} = S_0(n) + H(n)\frac{\delta a}{a_0^2}, \quad (29)$$

where S_0 is the strain data vector computed with the unstrained lattice constant a_0, and $H(n)$ is defined as the n^{th} component of a hydrostatic strain data vector *H*. Using the triangle inequality for vectors in the *n*-dimensional space, the norm of the strain data vector can be written as

$$\|S\| = \|N\epsilon\| = \left\|S_0 + H\frac{\delta a}{a_0^2}\right\| \leq \|S_0\| + \|H\|\left|\frac{\delta a}{a_0^2}\right|, \quad (30)$$

which shows that application of any $\tilde{a}_0$ except the a_0 will make the norm of $\|N\epsilon\|$ always greater than $\|S_0\|$. Therefore, iterating through the different lattice constants $a(\alpha)$ already measured in the range of azimuthal angle α, we determined the unstrained lattice constant a_0 as the parameter residing at the minima of the error function $E = \|S\|$, which is shown in Supporting Information Figure S9d. After determination of a_0 = 5.5715 Å for a poly-SiGe stripe laser-written at a speed of 0.1 mm s^{-1}, we solved equation (27) for a range of possible spatial configurations, including the slight rotations φ (∓2°) around the sample surface normal $z_{S\perp}$ and the experimental error in the incident angle β (10∓2°). At the optimum spatial configuration (β =9.88°, φ=-1.5°), which yields the best fit to the XRD data minimizing the shear strain component $|\epsilon_{xy}| \to 0$, we found the strain tensor as ϵ_{xx} = 0.75%, ϵ_{yy} = 0.30%, ϵ_{zz} = -0.13%, ϵ_{xy} = 0.00%. The in-plane strain, i.e., $\epsilon_{\parallel} = (\epsilon_{xx} + \epsilon_{yy})/2$= 0.53%, is in good agreement with the average in-plane strain $\epsilon_{\parallel}$ = 0.63∓0.2% measured by Raman spectroscopy on the laser-written stripes of 0.1 mm s^{-1} speed (see Figure 4d).

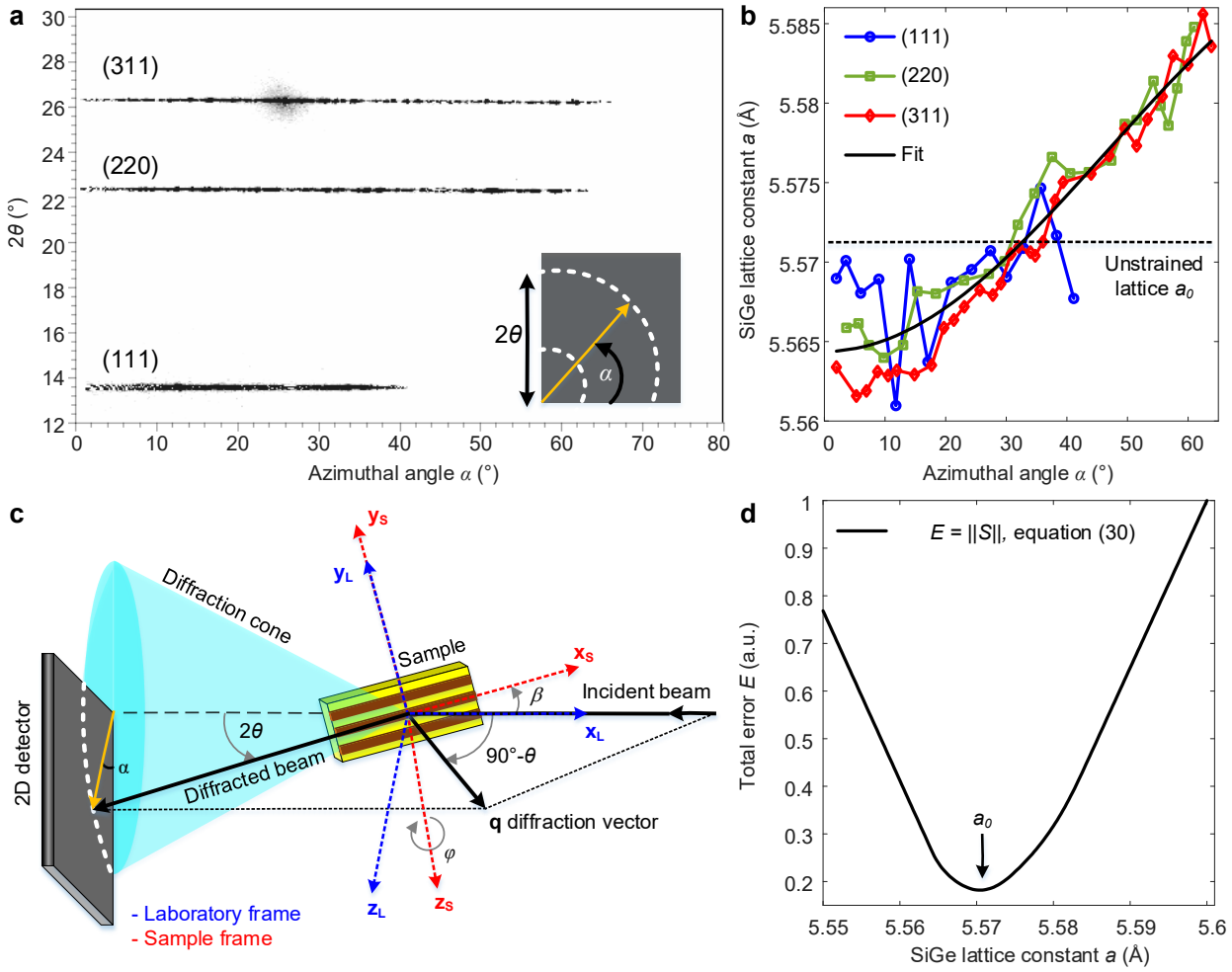

Figure S9: 2D strain analysis based on the azimuthal distortions of the XRD rings. a) Conversion of the XRD rings to lines *via* profiles in azimuthal sectors shows a slight decline in *2θ* over the azimuthal angle range, due to the residual biaxial strain in a laser-written stripe processed at a speed of 0.1 mm s^{-1}. **b)** The lattice constants *a(α),* which were calculated from the interplanar spacing d_{hkl} of the (111), (220) and (311) diffraction planes, are displayed for a better visualization of the distortion caused by the biaxial strain. The fits to the lattice constant *a(α)* were calculated from the estimated strain tensor ϵ (see Supporting Information Section S5). **c)** The schematic geometry used for the experiments and 2D strain analysis, showing the laboratory and sample coordinate frames. **d)** Total error function, which is taken as the norm of the estimated strain data vector ||S|| = ||Nϵ||, shows a minimum at the unstrained lattice constant a_0 for the XRD data set.

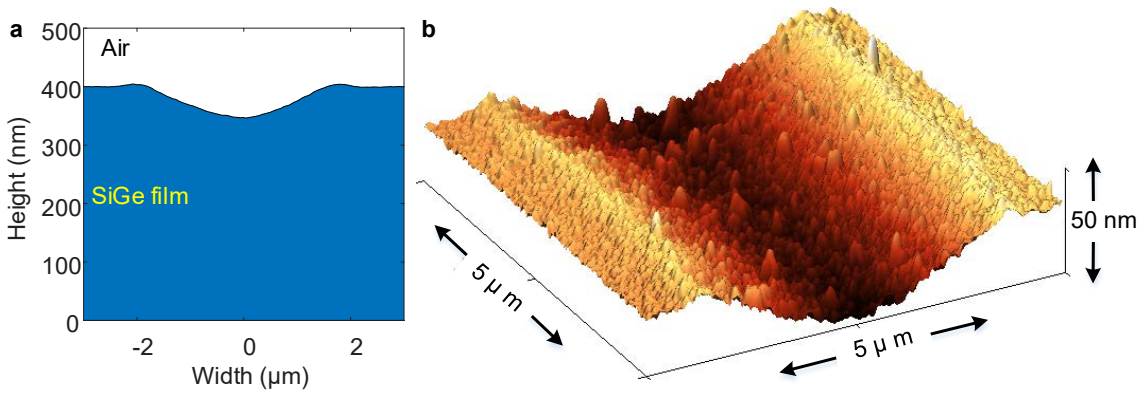

Figure S10: **Atomic force microscopy (AFM) on the laser-written SiGe stripes. a)** Topographical profile of the laser-processed a-SiGe shows the volume reduction after laser heating due to the higher density of poly-SiGe, as well as the effect of Marangoni flow on the surface. **b)** AFM image shows the surface topography for a laser-written poly-SiGe stripe of 0.1 mm s^{-1}. RMS roughness is 2.5 nm on the surface of the poly-SiGe stripes written at scan speeds of 0.1 and 1 mm s^{-1}, and it increases up to 10 nm for the higher scan speeds.

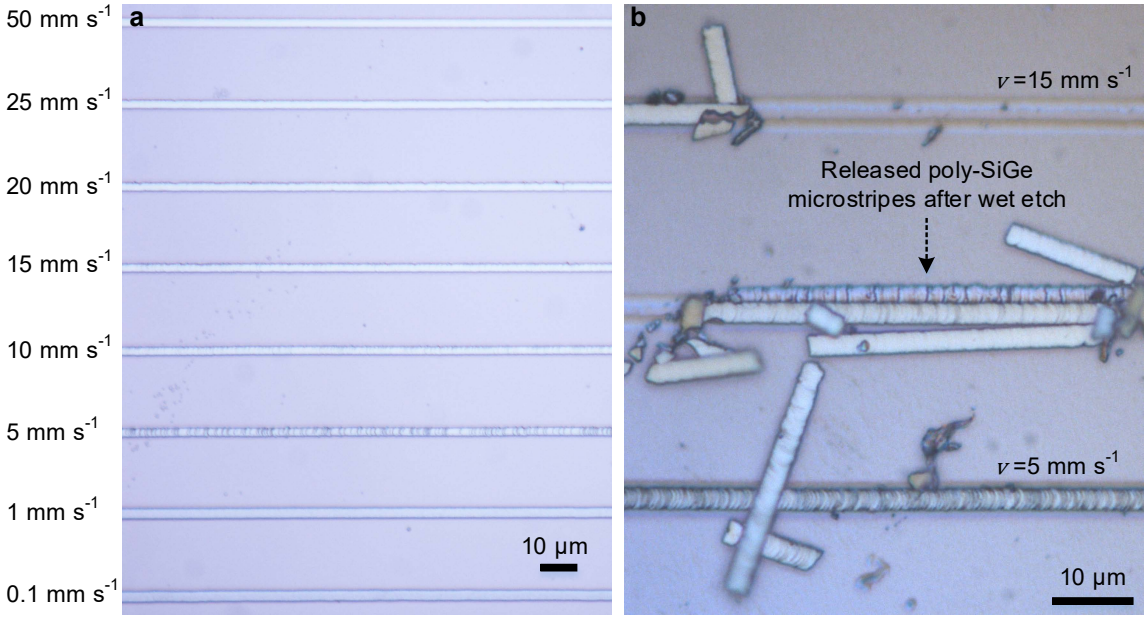

Figure S11: **Secco wet etching of the laser-written composition-graded poly-SiGe microstripes.** Results of Secco wet etch (potassium dichromate $K_2Cr_2O_7$ (3 Vol.%) + hydrofluoric acid HF (7 Vol.%) + DI water (90 Vol.%)) are shown in the figure for the laser-processed SiGe thin film of 400 nm thickness on a Si substrate. **a)** Optical microscope images show the laser-written SiGe stripes after Secco wet etching for 20 minutes. The potassium dichromate oxidizes weak Si-Si bonds, producing SiO_2, which is subsequently etched by HF. The etch rate monotonously decreases as the Ge composition *x* increases.[14] Si-rich regions are etched at a faster rate than Ge-rich regions, resulting in the under etching of the composition-graded microstructures produced on the top surface by laser-driven phase segregation. **b)** Released Ge-rich microstripes of nanometre thickness can be seen on the surface of the partially etched amorphous SiGe thin film after 30 minutes. Laser-written poly-SiGe microstripes produced at higher scan speeds are released first from the substrate during Secco wet etching, as their Si-rich under-cladding regions have higher etch rates.

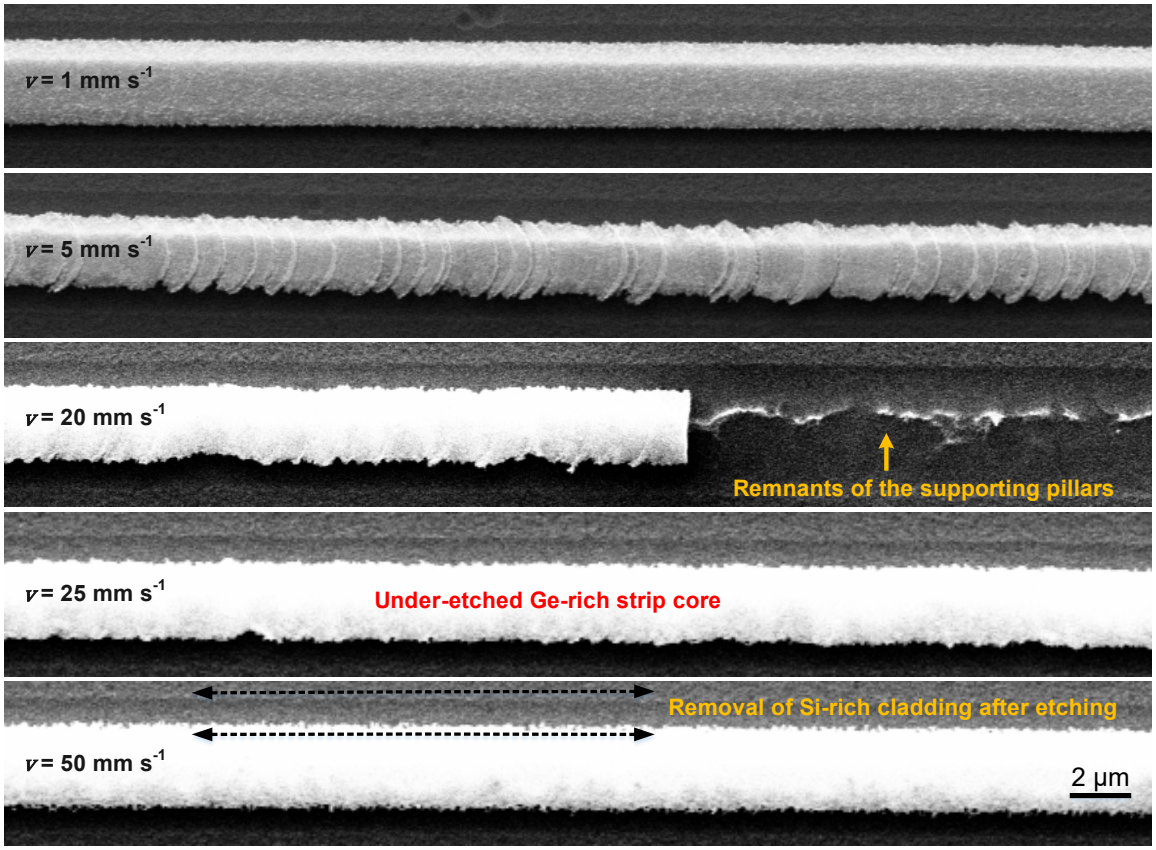

Figure S12: **SEM micrographs of Secco-etched poly-SiGe stripes laser-written at different scan speeds ranging from 1 to 50 mm s^{-1}.** Crescent-shaped micro-domains with Ge-rich outer nano-rings were observed on the poly-SiGe stripes laser written at the scan speed of 5 mm s^{-1}, which are ramifications of the explosive crystallization also observed in laser annealing of a-Si.[15] Under-etching of the composition-graded poly-SiGe microstripes can be seen from the broken part of the poly-SiGe microstripe produced at the scan speed of 20 mm s^{-1}. Si-rich under-cladding regions are etched away first, revealing the Ge-rich poly-SiGe strip cores supported by the pillars.

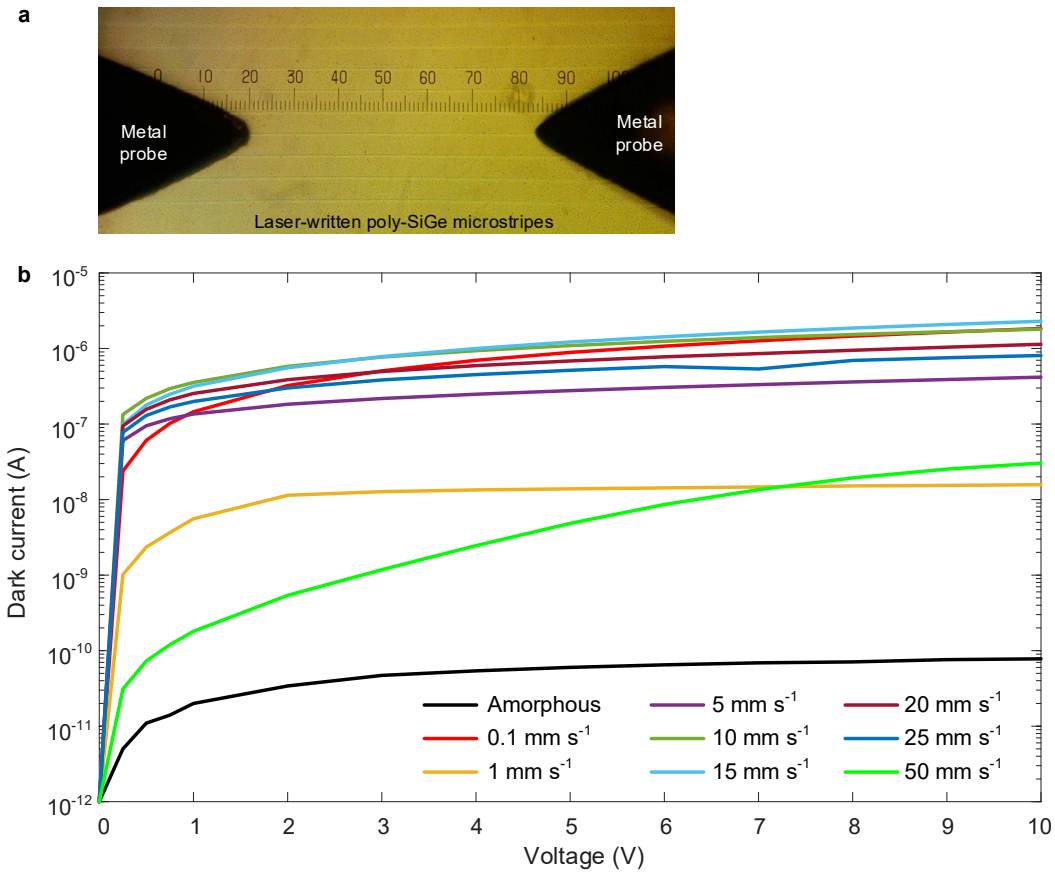

Figure S13: **Dark currents measured on a-SiGe region and laser-written poly-SiGe microstripes. a)** Top view optical microscope image showing the metal probes with microscopic tips positioned on the surface of laser-written SiGe microstripes. The length of the major divisions in the scale is 50 µm. **b)** Current (I)-voltage (V) characteristics were measured without illumination on the polycrystalline SiGe (poly-SiGe) microstripes laser-written at scan speeds ranging from 0.1 to 50 mm s^{-1}. To measure the dark currents on the amorphous regions, we placed two metal probes on the surface far from the laser-crystallized SiGe regions with a separation of 300 µm between them, which was kept the same for all I-V measurements. The dark currents are lower for the amorphous regions due to the higher electrical resistance in the amorphous material and can be lower by two to four orders of magnitude from those of the laser-written poly-SiGe microstripes. Saturation value of the dark currents I_0 is sensitive to the contact area of the metal probes; therefore, depending on the contact pressure, it can be lower or higher, as can be seen from the reduced dark current (yellow) of the SiGe microstripe written at a laser scan speed of 1 mm s^{-1}. We observed variations in the saturation currents in the range of 10^{-6}-10^{-8} A, depending on the mechanical loading of the metal probes. In addition, increased surface roughness observed at higher scan speeds can result in nanometre-scale air gaps, compromising the quality of metal-semiconductor physical contact. Therefore, reverse-bias current characteristics, which are determined by the thermionic emission and tunnelling mechanisms, could change depending on the surface state. For the SiGe microstripes written at a scan speed of 50 mm s^{-1}, we observed a tunnelling dominated dark current (green).

SI Section S6 - Estimation of the indirect bandgap of the unstrained SiGe alloy

The Ge molar fraction x and unstrained lattice constant a_0 of a $Si_{1-x}Ge_x$ alloy are related by Vegard's law as

$$a_0(x) = (1-x)a_{Si} + xa_{Ge} = 5.431 + 0.227x. \quad (31)$$

As the compositional spreading in the initial x_0 is low for the laser-written SiGe stripes of 0.1 mm s^{-1}, the unstrained lattice constant a_0 = 5.5715 Å can be determined by the XRD strain analysis explained in Supporting Information Section S5. Using equation (31), the corresponding Ge molar fraction was found to be x_0 =0.619 mol, which is close to the Raman estimated value of 0.604∓0.03 mol. The XRD analysis slightly overestimates the Ge molar fraction, due to the small deviations from Vegard's law.[16] Experimentally measured fundamental indirect bandgap of SiGe alloys as a function of Ge molar fraction x is given by[17]

$$E_g(x) = 1.155 - 0.43x + 0.206x^2 \text{ eV} \quad \text{for x < 0.85 (X band, Si-like),} \quad (32)$$

$$= 2.01 - 1.27x \text{ eV} \quad \text{for x > 0.85 (L band, Ge-like).}$$

Using equation (32), the fundamental indirect bandgap for the unstrained SiGe alloy is found to be $E_g(x_0)$ = 0.968 eV (λ = 1,281 nm).

SI Movies

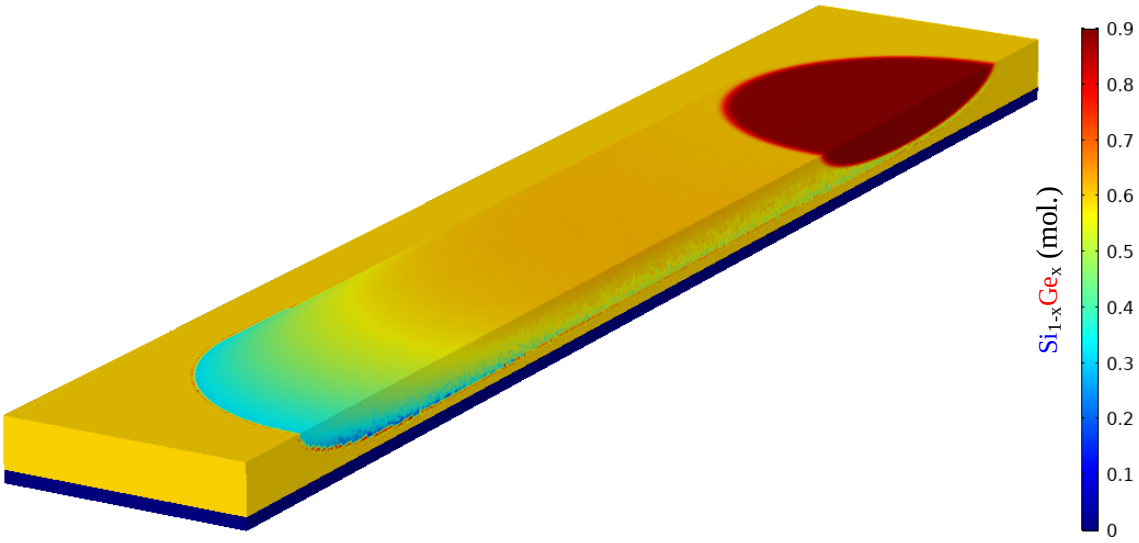

Movie S1 (separate file). Laser-driven phase segregation at the scan speed of 0.1 mm s^{-1}. Simulation of the laser-driven phase segregation in a-SiGe on Si shows the spatial and temporal evolution of the Ge molar fraction $x(\vec{r},t)$ during laser writing at a scan speed of 0.1 mm s^{-1}. Initial Ge composition is x_0 = 0.6 mol within the whole volume of the SiGe thin film. Only half of the simulation volume is shown due to the mirror symmetry. The laser-induced molten zone (red color) travels along the scan direction dragging the Ge-rich liquid, which solidifies at the trailing edge. After a Si-rich transient (cyan color), a steady-state region emerges with a Ge-rich strip core and a Si-rich under-cladding. Complete mixing occurs in the molten zone, which has a homogenous Ge distribution. The Si substrate (dark blue color) is also shown under the a-SiGe thin film of 400 nm thickness.

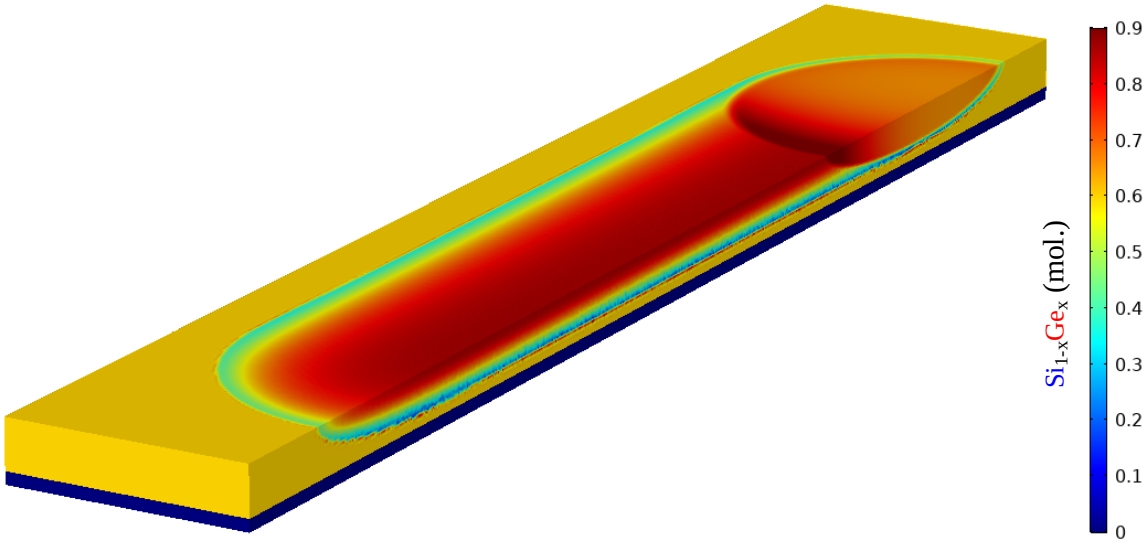

Movie S2 (separate file). Laser-driven phase segregation at the scan speed of 100 mm s^{-1}. Simulation of the laser-driven phase segregation in a-SiGe on Si shows the spatial and temporal evolution of the Ge molar fraction $x(\vec{r}, t)$ during laser writing at a scan speed of 100 mm s^{-1}. The initial Ge composition is x_0 = 0.6 mol across the whole volume of the SiGe thin film. Only half of the simulation volume is shown due to the mirror symmetry. The laser-induced molten zone (red color) travels along the scan direction dragging the Ge-rich liquid, which solidifies at the trailing edge. A build-up of Ge content *x* occurs at the trailing edge (darker red) of the traveling molten zone because of insufficient diffusion-limited Ge transport to reach complete mixing. After a very short Si-rich transient (cyan color), a steady-state region quickly emerges with a Ge-rich ($x > 0.6$) strip core and a Si-rich ($x < 0.6$) under-cladding. The composition gradient is higher than those achieved at lower scan speeds, due to the higher degree of phase segregation, which can be continuously controlled by the scan speed. The Si substrate (dark blue color) is also shown under the a-SiGe thin film of 400 nm thickness.

SI Tables

Table S1: Experimental data for the liquidus and solidus of SiGe alloys.[4]

x_S [mol]	0	0.1	0.209	0.384	0.597	0.754	1				
T_S [K]	1687	1609	1544	1442	1340	1283	1211				
x_L [mol]	0.105	0.206	0.255	0.377	0.404	0.496	0.602	0.6	0.747	0.754	0.896
T_L [K]	1665	1637	1620	1582	1578	1544	1506	1499	1431	1423	1325

Table S2: Parameter values used in the finite-element-method-based phase-field simulations of the $Si_{0.4}Ge_{0.6}$ alloy.[18-21]

Parameter	Value	Unit	Parameter	Value	Unit
Thickness of a-$Si_{0.4}Ge_{0.6}$ film	400	nm	Specific heat	482.9	J Kg^{-1} K^{-1}
Thickness of Si substrate	10	µm	Absorption coeff.	107430	cm^{-1}
Length	15	µm	Thermal cond. (solid)	2.8	W m^{-1} K^{-1}
Width	5	µm	Thermal cond. (liquid)	7	W m^{-1} K^{-1}
Diameter of the focused beam	3	µm	Diffusion coeff. D_L	3×10^{-8}	m^2 s^{-1}
Optical power *P*	250	mW	Diffusion coeff. D_S	0	m^2 s^{-1}
Initial Ge mole fraction x_0	0.6	mol	Melting temp. for Ge	1211.2	K
Reflection from Surface	0.46	-	Melting temp. for Si	1687.2	K
Solidus temp. (at x_0=0.6)	1337	K	Ideal gas constant *R*	8.314	J $mol^{-1}K^{-1}$
Liquidus temp. (at x_0=0.6)	1506	K	Latent heat of L_{Ge}/R	4441	K
Mean melting temp. T_m	1421.5	K	Latent heat of L_{Si}/R	6040	K
Mushy zone range ΔT_0	169	K	Regular mix. W_S/R	450	K
Latent heat of $Si_{0.4}Ge_{0.6}$	995.9	kJ kg^{-1}	Regular mix. W_L/R	800	K
Density of molten $Si_{0.4}Ge_{0.6}$	4510	Kg m^{-3}	Density of Si	2329	Kg m^{-3}
Density of solid $Si_{0.4}Ge_{0.6}$	4245.5	Kg m^{-3}	Thermal cond. of Si	135	W m^{-1} K^{-1}

SI References

1. Boettinger, W. J.; Warren, J. A.; Beckermann, C.; Karma, A. Phase-field Simulations of Solidification. *Annu. Rev. Mater. Res.* **2002**, *32*, 163–194.

2. De Oliveira, M. J. Equilibrium Thermodynamics; Rhodes, W. T., Stanley, H. E., Needs R., Eds.; Springer: Heidelberg, 2013; Ch. 10.

3. Bonham, B.; Guisbiers, G. Thermal Stability and Optical Properties of Si–Ge Nanoparticles. *Nanotechnology* **2017**, *28*, 245702.

4. Stohr, H.; Klemm, W. *Z.* Binary Systems with Ge: Ge−Al, Ge−Sn, and Ge−Si. Anorg. Allg. *Chem.* **1939**, *241*, 305–313.

5. La Magna, A.; Alippi, P.; Privitera, V. A Phase-Field Approach to the Simulation of the Excimer Laser Annealing Process in Si. *J. Appl. Phys.* **2004**, *95*, 4806–4814.

6. Moelans, N.; Blanpain, B.; Wollants, P. An Introduction to Phase-Field Modeling of Microstructure Evolution. *CALPHAD: Comput. Coupling Phase Diagrams Thermochem.* ***2008****, 32*, 268–294.

7. Kurz, W.; Fisher, D. J. Fundamentals of Solidification; Trans Tech Publications: Aedermannsdorf, 1992; Ch.3.

8. Perova, T. S.; Wasyluk, J.; Lyutovich, K.; Kasper, E.; Oehme, M.; Rode, K.; Waldron, A. Composition and Strain in Thin $Si_{1-x}Ge_x$ Virtual Substrates Measured by Micro-Raman Spectroscopy and X-ray Diffraction. *J. Appl. Phys.* **2011**, *109*, 033502.

9. Rouchon, D.; Mermoux, M.; Bertin, Hartmann, F. J. M. Germanium Content and Strain in $Si_{1-x}Ge_x$ Alloys Characterized by Raman Spectroscopy. *J. Cryst. Growth* ***2014****, 392*, 66–73.

10. Pezzoli, F.; Bonera, E.; Grilli, E.; Guzzi, M.; Sanguinetti, S.; Chrastina, D.; Isella, G.; von Kanel, H.; Winterberger, E.; Stangl, J.; Bauer, G. Raman Spectroscopy Determination of Composition and Strain in $Si_{1-x}Ge_x$/Si Heterostructures. *Mater. Sci. Semicond. Process.* **2008**, *11*, 279–284.

11. Lockwood, D. J.; Baribeau, J.-M. Strain-Shift Coefficients for Phonons in $Si_{1-x}Ge_x$ Epilayers on Silicon. *Phys. Rev. B* **1992**, *45*, 8565–8571.

12. Wang, D.; Chen, N.; Chen, Z.; Zhao, Z.; Pang, F.; Wang, T. Composition and Strain Analysis of $Si_{1-x}Ge_x$ Core Fiber with Raman Spectroscopy. *AIP Adv.* **2018**, *8*, 065006.

13. Ramirez-Rico, J.; Lee, S.-Y.; Ling, J. J.; Noyan I. C., Stress Measurement Using Area Detectors: A Theoretical and Experimental Comparison of Different Methods in Ferritic Steel Using a Portable X-ray Apparatus. *J. Mater. Sci.* **2016**, *51*, 5343–5355.

14. Abbadie, A.; Allibert, F.; Brunier, F. Defect Delineation and Characterization in SiGe, Ge and Other Semiconductor-on-Insulator Structures *Solid-State Electron.* **2009**, *53*, 850–857.

15. Boyd, I. W. A Review of Laser Beam Applications for Processing Silicon. *Contemp. Phys.* **1983**, *24*, 461–490.

16. Kasper, E.; Schuh, A.; Bauer, G.; Hollander, B.; Kibbel, H. Test of Vegard's Law in Thin Epitaxial SiGe Layers. *J. Cryst. Growth* ***1995****, 157*, 68–72.

17. Weber, J.; Alonso, M. I. Near-Band-Gap Photoluminescence of Si-Ge Alloys. *Phys. Rev. B* **1989**, *40*, 5683–5693.

18. Adachi, S. Properties of Semiconductor Alloys: Group-IV, III–V and II–VI Semiconductors; Capper, P., Kasap, S., Willoughby, A., Eds.; Wiley: Wiltshire, 2009, Ch.2.

19. Ricci, E.; Amore, S.; Giuranno, D.; Novakovic, R.; Tuissi, A.; Sobczak, N.; Nowak, R.; Korpala, B.; Bruzda, G. Surface Tension and Density of Si-Ge Melts. *J. Chem. Phys.* **2014**, *140*, 214704.

20. Cheaito, R.; Duda, J. C.; Beechem, T. E.; Hattar, K.; Ihlefeld, J. F.; Medlin, D. L.; Rodriguez, M. A.; Campion, M. J.; Piekos, E. S.; Hopkins, P. E. Experimental Investigation of Size Effects on the Thermal Conductivity of Silicon-Germanium Alloy Thin Films. *Phys. Rev. Lett.* **2012**, *109*, 195901.

21. Wang, Q.; Chang, J.; Wang, H. P. Thermophysical Properties and Atomic Structure of Liquid Si-Ge Alloys. *Mater. Chem. Phys.* **2019**, *221*, 224–231.